ROYAL SOCIETY
OF CHEMISTRY

PAPER

Check for updates

Electronic, optical and structural properties of MnPS₃: advanced spectroscopy and theoretical investigation†

K. Ignatowicz, [iD] [a] W. M. Linhart, [iD] *[a] M. Rybak,[a] N. Antonatos,[a] B. Wu, [iD] [b] J. Luxa,[b] J. Serafińczuk,[c] M. Peter,[a] Z. Sofer [iD] [b] and R. Kudrawiec [iD] [a]

In the field of van der Waals semiconductor research, studying antiferromagnetic order in materials like MnPS₃ has highlighted potential applications in heterostructures. This research examines the detailed correlations between the optical and magnetic properties of MnPS₃, providing insights into its behavior across various temperatures. Using advanced spectroscopic methods such as photoreflectance (PR) and absorption, significant optical transitions, labeled as E_1, E_2, E_3, and E_G, have been identified in bulk MnPS₃. These transitions are characterized by detailed analysis, highlighting their responses to temperature changes. Structural data from X-ray diffraction reveal how lattice parameters evolve with temperature, influencing magnetic phase transitions in MnPS₃. Understanding how optical transitions correlate with structural changes offers deeper insights into their joint influence on the optical and magnetic properties, paving the way for advances in spintronic and magneto-optical technologies. These results underscore the importance of investigating the nuanced optical and magnetic behaviors of MnPS₃ and emphasize the ongoing research needed to unlock the full potential of these layered materials for future technological innovations.

1 Introduction

Recently, van der Waals semiconductors have gained significant attention due to their versatile scientific applications. These materials exhibit remarkable traits such as flexible surfaces,[1] ultrathin layers,[2] high mobilities,[3] strong in-plane anisotropy,[4] and tunable band gaps.[5] Transition metal phosphorus trichalcogenides (TMPTs), expressed as MPX₃ (where M = V, Mn, Fe, Co, or Ni and X = S or Se), represent a new class of 2D van der Waals antiferromagnetic semiconductors, maintaining intrinsic ordering even in monolayer or few-layer forms.[6–8] Antiferromagnetic materials possess unique functionalities that can arise from subtle secondary magnetization or polarization states. At a critical temperature, known as the Néel temperature (T_N), the magnetization can transition from

antiferromagnetic to paramagnetic, leading to a reorganization of spin orientations. The MPX₃ category features tunable band gaps within the range of 1.3 to 3.5 eV.[9] While some MPX₃ crystals share a similar monoclinic structure with the $C2/m$ space group, their magnetic properties vary according to the transition metal used. Notably, MnPS₃, FePS₃, and NiPS₃ exhibit distinct magnetic orderings—Heisenberg-type, Ising-type, and XXZ-type, respectively—affecting their magnetic susceptibilities and local electron dynamics.[10] FePS₃, with $T_N \approx 118$ K, stands out for its strong optical transitions within the visible spectrum, boasting a band gap between 1.5 eV and 1.8 eV,[11–13] making it suitable for photodetection applications. MnPS₃ (with $T_N \approx 78$ K), characterized by significant excitonic effects and a band gap of around 3.0 eV,[14,15] is advantageous for optoelectronic applications due to its high sensitivity to ultraviolet light. Additionally, NiPS₃ (with $T_N \approx 155$ K) demonstrates increased nonlinear optical susceptibility, enhancing its utility in photonic applications owing to its unique magnetic interactions and structure.[16,17] Advances in experimental techniques and computational modeling reveal that these materials retain their unique magnetic ordering even at monolayer thickness, thereby elevating their potential for next-generation spintronic and optoelectronic technologies.[7]

Since the 1980s, bulk MnPS₃ has garnered significant interest due to its unique characteristics as a two-dimensional

[a] Department of Semiconductor Materials Engineering, Faculty of Fundamental Problems of Technology, Wrocław University of Science and Technology, Wybrzeże Wyspiańskiego 27, 50-370 Wrocław, Poland. E-mail: wojciech.linhart@pwr.edu.pl

[b] Department of Inorganic Chemistry, University of Chemistry and Technology Prague, Technická 5, 166 28 Prague 6, Czech Republic

[c] Department of Nanometrology, Faculty of Electronics, Photonics and Microsystems, Wrocław University of Science and Technology, Wybrzeże Wyspiańskiego 27, 50-370 Wrocław, Poland

magnetic semiconductor. Research by Ouvrard *et al.* has demonstrated that the crystal structures of various MPS$_3$ phases exhibit significant variations in lattice parameters and symmetry, which are influenced by the specific transition metal involved; this finding highlights the crucial role of van der Waals forces in stabilizing these layered structures.[18] Their work indicates that varying stoichiometries can affect the physical properties of these materials, a key consideration for tailoring them for specific applications. Building on these insights, Brec's review provides valuable perspectives on the chemical properties and possible applications of MPS$_3$ materials, reinforcing the versatility of transition metal phosphorous trisulfides in electronics and catalysis.[19] Initial studies suggested that intercalating different guest cations could adjust the magnetic characteristics of MnPS$_3$, while maintaining an antiferromagnetic state below approximately 78 K.[20] Further research has confirmed its semiconductor nature with a band gap close to 1.3 eV,[21] establishing its potential in optoelectronic applications. Recent advancements in spectroscopic techniques, especially Raman spectroscopy, have provided deeper insights into its vibrational and electronic transitions.[22] Moreover, research conducted in the 2010s revealed excitonic effects due to tightly bound electron–hole pairs, affirming its potential for high-excitation applications.[23] Density functional theory (DFT) simulations further elucidated its robust p-type semiconductor properties and enhanced transport characteristics.[24,25]

Recent findings emphasize the interplay between magnetic ordering and optical properties, leading to unique functions such as linear magneto-electric phases that persist in monolayers, suggesting significant potential for the development of advanced opto-spintronic devices.[26,27] Alloying MnPS$_3$ with Zn offers opportunities for tunable band gaps and optical properties,[28] potentially resulting in engineered materials with specific electronic features. Ongoing research on bulk MnPS$_3$ underscores its relevance in the fields of magnetism and optoelectronics. As an antiferromagnetic substance, MnPS$_3$ enables the manipulation of electron spin, allowing for the development of energy-efficient spintronic transistors with high performance. Additionally, due to its magneto-optical effect, MnPS$_3$ can alter its optical properties in response to external magnetic fields, making it an attractive candidate for magneto-optical sensors capable of detecting changes in magnetic fields. However, further research on the electrical and optical properties of MnPS$_3$, along with its integration with other materials, is essential to fully harness its potential in practical technological applications. Moreover, the fabrication of devices utilizing MnPS$_3$ presents challenges, notably the difficulty in achieving high-quality single crystals or thin films, integration with other semiconductor materials due to lattice mismatches, and the need for new fabrication techniques tailored to MnPS$_3$, as conventional methods might not apply.[29,30] Additionally, concerns regarding the stability of MnPS$_3$ in adverse environmental conditions, along with challenges in scaling production processes for uniformity and cost-effectiveness, underscore the necessity for further research into its fundamental properties to enhance device performance in potential applications including spintronics and magneto-optics.[23,31–33]

The band gap of MnPS$_3$ has been the subject of extensive study due to its implications for optoelectronic applications. Reported values of the band gap vary significantly based on experimental conditions and theoretical approaches. One study using density functional theory calculations found a band gap of approximately 2.44 eV, indicating that the electronic structure can be adjusted across different phases, including the Janus phase.[34] Another research noted a broader range, identifying a band gap of about 3.0 eV, which positions MnPS$_3$ as a promising p-type semiconductor for ultraviolet light detection.[35] Absorption measurements revealed an effective direct band gap of around 1.3 eV, corresponding to mid-infrared emissions tied to the d-state transitions of Mn(II) during recombination processes.[28] Temperature-dependent studies suggested that the fundamental optical absorption band softens with increasing temperature, leading to a reduction in the band gap, crucial for understanding the material's performance under various thermal conditions.[36] Advanced techniques such as ARPES have further confirmed alterations in the band structure during the antiferromagnetic phase transition of MnPS$_3$, reflecting the complexity of its electronic properties and the potential for tuning the band gap through external influences.[37]

The interplay between the magnetic and optical properties is particularly promising for magneto-optics and magnetic storage applications.[38,39] Numerous advancements have highlighted the significance of this relationship for spintronics and magnetoresistive memory technologies.[40,41] However, research on magneto-optics in MnPS$_3$ remains relatively limited. Unlike traditional methods such as neutron scattering and vibrating sample magnetometry, vibrational spectroscopy offers a fresh perspective for observing magnetic phase transitions. Strong spin–phonon and spin–photon coupling during magnetic-order phase transitions enable indirect detection, especially notable in temperature-dependent behaviors.[6,7] These couplings can arise from direct exchange interactions, distortion effects, or spin–lattice coupling, influencing the strength of magnetic interactions and modifying transition temperatures as well as phase stability. As temperatures increase, enhanced phonon activity can disrupt magnetic order, leading to transitions from antiferromagnetism to paramagnetism, thereby impacting the relaxation dynamics and energy dissipation processes of spins.[26] Additionally, magneto-optical interactions can be explored through various optical measurements, including photoluminescence, photothermoreflectance, phototransmission, and optical absorption. Recent studies have demonstrated a significant correlation between magnetic ordering and photo-emission in layered MnPS$_3$, even down to monolayer thicknesses.[26] Observations reveal that photoluminescence intensity and defect emission peak positions exhibit critical behavior at the Néel temperature, suggesting the independence of these behaviors from the monolayer to bulk thickness. Despite initial discoveries regarding layered MnPS$_3$, understanding the intricate structural, optical, and band-edge transition behaviors near the antiferromagnetic-to-paramagnetic transition temperature (T_N = 78 K)[42] remains a crucial area that requires further exploration.

This journal is © The Royal Society of Chemistry 2025

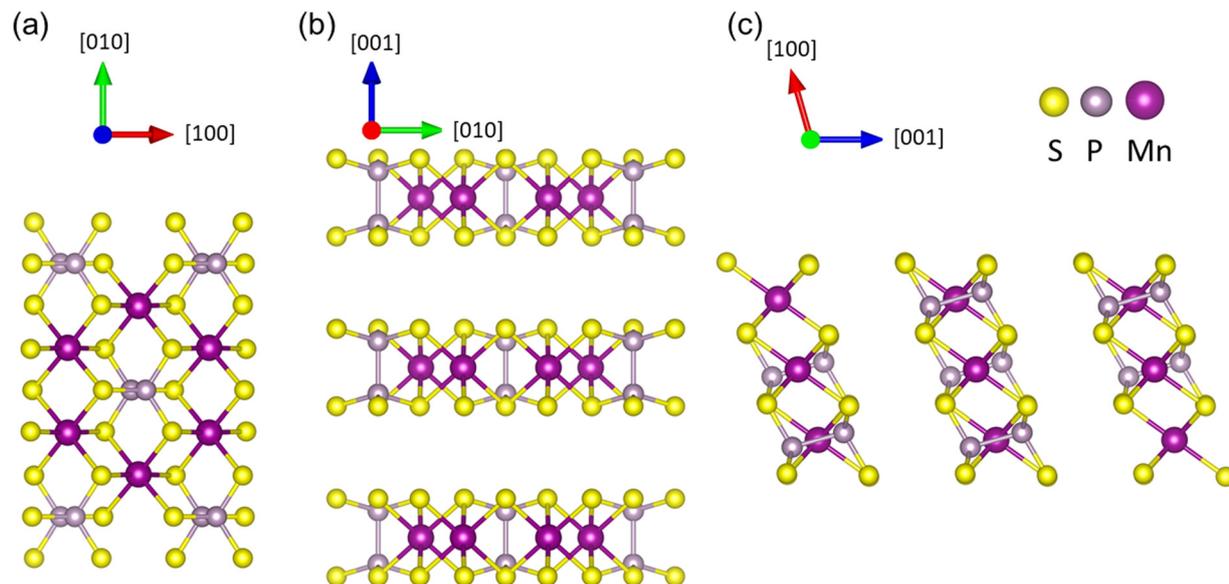*J. Mater. Chem. C*, 2025, **13**, 9194–9203 | **9195**

Fig. 1 Different crystal orientations for MnPS$_3$. The (a) [001], (b) [100], and (c) [010] directions are pointing out of the page for the space group C2/m. In panels (b) and (c) the layered structure can be seen clearly, and the van der Waals interactions between these layers can be distinguished.

The temperature dependence of the band-gap energy in semiconductors represents a fundamental property of considerable practical and theoretical interest. In conventional semiconductors, such as those from the III–V family, the band gap typically decreases monotonically with an increase in temperature due to lattice expansion and temperature-dependent electron–phonon interactions. Various models exist to describe this temperature dependence, including the Bose–Einstein, Varshni, Pässler, and O'Donnell models.[43–47] Unlike III–V semiconductors, MnPS$_3$ has a layered structure (see Fig. 1), consisting of Mn^{2+} cations coordinated by sulfur atoms within a van der Waals framework. Its structural and bonding characteristics play a crucial role in its electronic and magnetic behavior, as discussed more in detail in the Results and discussion section. In this study, we investigate how changes in magnetic ordering influence the temperature dependence of the band gap in MnPS$_3$. This research employs photoreflectance measurements, which are sensitive to direct transitions, along with absorption and X-ray diffraction techniques, all supported by DFT+U studies.[48] This comprehensive approach aims to enhance our understanding of the phenomena governing the interplay between magnetic and optical properties in this promising material, paving the way for future advancements in semiconductor technologies and applications.

2 Experimental and computational details

The bulk MnPS$_3$ crystal for this study was grown by chemical vapor transport through the direct reaction of pure Mn, P, and S elements in a quartz ampoule. Details of the material synthesis and structural characterization of MnPS$_3$ can be found in the ESI.†

For PR and absorption experiments, the sample was illuminated with a halogen lamp, and the reflected light was dispersed using a single grating monochromator with a focal length of 0.55 m. A Si photodiode was used to detect the resulting signal, and the lock-in technique was employed for measurement. Reflectance modulation was achieved by using a laser beam with a wavelength of 405 nm and a frequency of 280 Hz. Throughout all the optical measurements, the sample was positioned on a cold finger within a closed cycle refrigerator, which was connected to a programmable temperature controller capable of accommodating measurements in the 10–300 K temperature range.

X-Ray diffraction curves were obtained using a Malvern PANalytical Empyrean diffractometer supported with a PIXcel3D detector. For all measurements, a Bragg–Brentano optics configuration and CuKα1 = 1.540597 radiation source were used. Measurements at low temperatures were made using an Oxford Cryosystems PheniX chamber. This equipment enables a temperature range from 298 K to 12 K with a temperature uniformity across the sample of 0.1 degrees. The sample for measurement was ground to obtain homogeneity and to obtain as many reflections as possible. XRD analysis was performed on MnPS$_3$ in an angular range of 10 to 90 degrees, with a step size of 0.0131 degrees. Temperature-dependent XRD diffractograms were acquired at 20 K intervals, spanning 33 to 300 K. A stabilization period of 20 minutes was implemented after each temperature adjustment to ensure the precision and consistency of the measurements. Corrections were applied to account for variations in the height of the measuring table induced by temperature fluctuations. The system was calibrated using a silicon standard (NIST 640b). The obtained diffraction patterns were compared with the reference pattern for MnPS$_3$ listed in the JCPDF card no. 00-033-0903.

X-Ray photoelectron spectroscopy (XPS) measurements were performed using an ESCAProbeP spectrometer (Omicron Nanotechnology Ltd, Germany) employing a monochromatic aluminum X-ray radiation source (1486.7 eV). Wide-scan surveys of all

9196 | J. Mater. Chem. C, 2025, **13**, 9194–9203

This journal is © The Royal Society of Chemistry 2025

elements were performed with subsequent high-resolution scans of manganese (Mn 2p), phosphorus (P 2p), and sulfur (S 2p). The samples were placed on a Si wafer. An electron gun (1–5 V) was utilized to eliminate the sample charging during measurement. All XPS survey spectra were afterwards analyzed using CasaXPS software.

Calculations based on density functional theory (DFT) were carried out using the Vienna *Ab initio* Simulation Package (VASP).[49] The interactions between electrons and ions were treated using the projector-augmented wave (PAW) method.[50] The Perdew–Burke–Ernzerhof (PBE) exchange–correlation functional was employed.[51] A plane wave basis with a cut-off energy of 550 eV was used, along with a Monkhorst–Pack k-point sampling grid of $12 \times 12 \times 8$ for Brillouin Zone integrations,[52] employing Gaussian smearing with a width of 0.02 eV.

All calculations took into account the spin–orbit coupling (SOC) and long-range magnetic order – originating from the half-filled 3d orbitals of manganese states. For the ground state, the antiferromagnetic Néel-type magnetic order reported in the literature was assumed, with the quantization axis of magnetic moments consistent with experimental observations.[53] To account for van der Waals interactions, the semi-empirical D3 Grimme approach was utilized.[54] Structural optimizations, including atomic positions and lattice parameters, were performed using Dudarev's approach to DFT+U methodology,[55] which applies Hubbard U parameters to model on-site Coulomb interactions for 3d electrons in transition metals (to replicate the geometric structure reported in the literature and avoid forces/strains in the system). A U value of 1.8 eV was chosen to evaluate optical transitions.[37] Direct interband momentum matrix elements were calculated through wave function derivatives using density functional perturbation theory.[56] To simulate a phase resembling a paramagnetic state, the system was expanded into a $3 \times 3 \times 2$ supercell. The spin magnetic moments on manganese ions were randomly oriented, ensuring that their magnitudes remained constant and that the total net magnetic moment was zero. The impact of this operation on the geometric structure of the system was neglected. The band structure was then calculated, including spin–orbit interaction, and subsequently unfolded onto a primitive cell to derive the effective band structures.[57,58]

3 Results and discussion

The monoclinic structure of $MnPS_3$ is illustrated in Fig. 1. The crystal is characterized by parallel planes of Mn^{2+} cations separated by two planes of sulfur atoms. Each Mn^{2+} ion is octahedrally coordinated by six sulfur atoms, forming trigonally distorted MnS_6 octahedra. Within each $MnPS_3$ layer, Mn^{2+} cations and $[P_2S_6]^{4-}$ anions are linked together by Mn–S bonds, with the P_2S_6 units exhibiting near-octahedral coordination. The Mn–S bonds are predominantly ionic, while the P–S bonds within the $[P_2S_6]^{4-}$ units are covalent. The layered structure is stabilized by weak van der Waals interactions between adjacent sulfur planes, defining $MnPS_3$ as a van der Waals material.

Table 1 Overview of $MnPS_3$ crystallographic parameters

Lattice parameters of $MnPS_3$	
Crystal structure	Monoclinic
Space group	$C2/m$ (12)
a	6.08 Å
b	10.52 Å
c	6.80 Å
α	90.0°
β	107.35°
γ	90°
Cell volume	414.79 Å^{-3}

The geometric parameters of the $MnPS_3$ structure are listed in Table 1.

To experimentally validate the microstructure and chemical composition of the $MnPS_3$ sample, we performed the characterization of the exfoliated crystal flakes using EDX and XPS techniques. The percentages of atomic concentration (at%) obtained from standardless EDS quantification are 62.3% for S, 20.7% for P, and 17% for Mn. These detected values fall within the acceptable experimental range and confirm that the measured stoichiometry of the crystal corresponds to $MnPS_3$, as expected. Additional EDS spectra and quantification results are provided in Fig. S1 of the ESI.† These experimental findings conclusively demonstrate that the obtained crystals are $MnPS_3$.

The $MnPS_3$ surface composition was investigated through XPS. The wide-survey spectrum confirmed the presence of manganese, phosphorus, and sulfur in addition to adventitious carbon and oxygen due to partially oxidized species (Fig. S2 in the ESI†). The Mn 2p profile revealed two oxidation states of manganese, namely Mn^{2+} and Mn^{3+}. The two highest peaks of the spectrum, assigned to the Mn 2p$_{3/2}$ and Mn 2p$_{1/2}$ orbitals, were both deconvoluted into Mn^{2+} and Mn^{3+} at 636.0 and 637.4 eV for 2p$_{3/2}$, and 647.4 and 648.8 eV for 2p$_{1/2}$, respectively. Furthermore, two satellite peaks at 640.9 and 653.8 eV emerged as a result of the interaction of 3p–3d at the optical absorption[59] (Fig. S3 in the ESI†). The XPS spectrum of P 2p was fitted with two peaks corresponding to P 2p$_{3/2}$ and P 2p$_{1/2}$ orbitals at 131.5 and 132.4 eV, respectively. The absence of any peaks related to oxidized phosphorus is indicative of the good stability of $MnPS_3$ under ambient conditions (Fig. S3 in the ESI†). Lastly, the S 2p high-resolution XPS peak was deconvoluted into S 2p$_{3/2}$ and S 2p$_{1/2}$ with a spin–orbit coupling of 1.16 eV (Fig. S3 in the ESI†).

The PR, absorption, and PL spectra for a bulk $MnPS_3$ acquired at 20 K are depicted in Fig. 2. By combining these experimental methods, we can clearly determine the optical transitions of $MnPS_3$ and ascertain their energy levels. In the PR spectrum, four resonances, labeled as E_1, E_2, E_3, and E_G, are visible. The explanation for these optical transitions will be provided subsequently.

To ascertain the resonance's position on the energy scale and its broadening, we employed the Aspnes formula for fitting the PR spectrum:

$$\frac{\Delta R}{R}(E) = \mathrm{Re}\left[\frac{A \exp(i\theta)}{(E - E_t + i\Gamma)^m}\right]. \tag{1}$$

This journal is © The Royal Society of Chemistry 2025

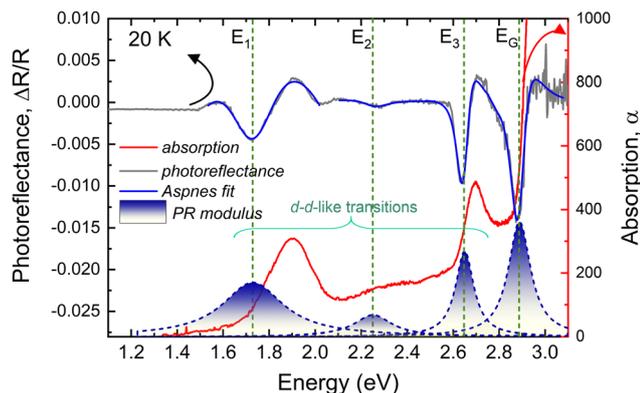*J. Mater. Chem. C*, 2025, **13**, 9194–9203 | **9197**

Fig. 2 Photoreflectance and optical absorption spectra of MnPS$_3$ collected at 20 K. Aspnes fit to the PR spectrum is also included, and the moduli of the PR transitions are plotted as green-shaded Lorentzian curves.

In this equation, $\Delta R/R$ represents the energy dependence of the PR signal. Here, A stands for the amplitude of the resonance, E_t denotes the energy of the optical transition, Γ represents the broadening parameter, and θ signifies the phase of the resonance line.[60] The parameter m is contingent upon the nature of the optical transition; conventionally, $m = 2.5$ is utilized for band-to-band transitions, whereas $m = 2$ is designated for excitonic transitions. To provide a clearer depiction of the energy transitions, their moduli are depicted in Fig. 2 below the PR spectrum (indicated by the dashed-line envelopes at the bottom), which are defined by the equation:

$$\Delta\rho(E) = \frac{|A|}{\left[(E - E_t)^2 + \Gamma^2\right]^{\frac{m}{2}}}. \tag{2}$$

Since PR is only sensitive to direct optical transitions, and the PR resonance spans the absorption spectrum, we can conclude that all measurements presented here reveal the direct character of the optical transitions. The absorption spectrum, taken at 20 K exhibits several intriguing features around 1.8–1.9 eV, 2.1–2.5 eV, 2.6–2.7 eV, and 3.0 eV. Each absorption feature is represented in the PR spectrum, denoted as E_1, E_2, E_3, and E_G, respectively. The absorption spectra of transition metal compounds are typically elucidated by two distinct types of transitions: one involves electron motion within the partially occupied outer d shell of the transition metal ion, termed "crystal-field" transitions, while the other comprises more pronounced ultraviolet excitation, where electron transfer between ligands and the metal occurs, known as "charge-transfer" transitions. Similar transitions have previously been observed in absorption studies by Grasso et al.[61] and in microthermal-modulated reflectance experiments by Ummah et al.;[62] however, no measurements were conducted using classical photoreflectance techniques. E_1, E_2, E_3, and E_G represent the $^6A_{1g} \rightarrow\ ^4T_{1g}$, $^6A_{1g} \rightarrow\ ^4T_{2g}$, $^6A_{1g} \rightarrow \{^4E_g, ^4A_{1g}\}$, and $^6A_{1g} \leftarrow$ P,S $3p_xp_y$ transition energy, respectively to the Mullikan notation.[61]

There are several studies on the band structure calculations of MnPS$_3$ in the literature.[63,64] A standard approach to account for the localization of correlated states originating from the half-filled manganese 3d orbitals is to include the Hubbard correction or to use hybrid functionals (due to the exact Hartree–Fock exchange), and both types of results have been reported[23,53] (note that neglecting either localization or spin polarization may lead to the closure of the band gap, as the 3d states, which are otherwise well separated, become pinned at the Fermi level). The most common issue when using DFT+U is the lack of a priori knowledge of the U parameter value, which often necessitates exploring a range of U values. However, for bulk MnPS$_3$, previous studies have reported a comparison between DFT+U (in the Dudarev formalism) and experimental ARPES data, which enabled the determination of a specific value of $U_{eff} = 1.8$ eV.[37] This allowed us to employ the same model parameters to accurately reproduce the ground state (Néel-type antiferromagnetic order), while ensuring an excellent agreement with the experimental band structure (and excitations[28]), at a lower computational cost compared to hybrid functionals.

To elucidate the observed optical transitions in the bulk phase below T_N, we present the band structure calculations in Fig. 3(a), which are plotted along the high-symmetry lines in the first Brillouin zone. The valence band maximum (VBM) is located at the Y point, whereas the conduction band minimum (CBM) is found at the K point, indicating the indirect nature of the band gap. It is noteworthy that the energy difference between the direct band gap at the K point and the indirect band gap is approximately 0.166 eV. Utilizing the calculated oscillator strength and photoreflectance measurements, we were able to determine the highly probable optical transitions at 20 K; $E_1 = 1.8$ eV (from absorption 1.71 eV), $E_2 = 2.25$ eV (from absorption 2.27 eV), $E_3 = 2.66$ eV (from absorption 2.65 eV) and $E_G = 2.87$ eV (from absorption 2.89 eV). These transitions can be assigned to transitions K^1, Y_2^1, Y_2^2 and L^4, respectively, in Fig. 3(b). However, additional transitions may also be possible due to the complex band structure of this material, which includes a large number of high symmetry points in the Brillouin zone. This results in singularities in the total optical density of states, to which photoreflectance spectroscopy is particularly sensitive.

The temperature dependence of the optical transition of MnPS$_3$ has also been comprehensively investigated. For this purpose, PR and absorption measurements have been performed in the temperature range from 20 to 300 K. Fig. 4(a) shows the PR spectra and the corresponding fits of MnPS$_3$ measured at temperatures between 20 and 300 K in the 1.15–1.65 eV energy range. The transition energies E_1, E_3, and E_G at each temperature were determined by fitting the spectra with eqn (1). The transition E_2 has not been analyzed because it was clearly visible only at very low temperatures and almost invisible at higher temperatures. It can be observed that the positions of the E_3 and E_G PR resonances move toward lower energies and broaden as the temperature increases. Surprisingly, the E_1 resonance shifts slightly to higher energies.

Fig. 4(b) shows absorption spectra recorded at temperatures between 20 and 300 K. At low temperatures, below T_N, three
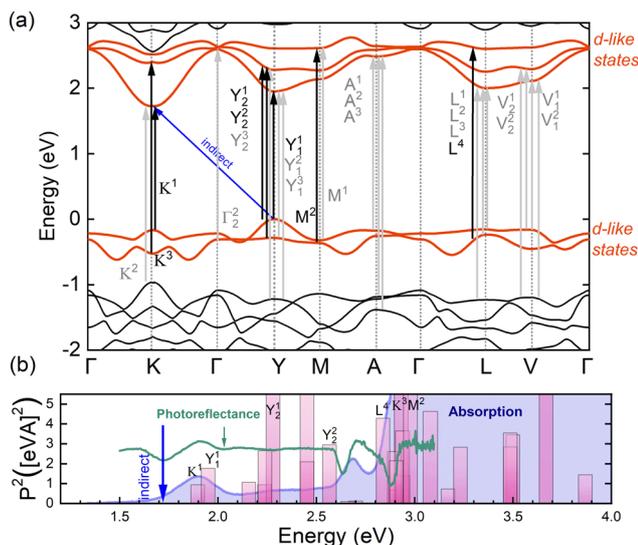
9198 | J. Mater. Chem. C, 2025, **13**, 9194–9203

This journal is © The Royal Society of Chemistry 2025

Fig. 3 (a) The electronic structure for the magnetic ground state (A-type antiferromagnetic, A-AFM) of bulk $MnPS_3$ is depicted along high-symmetry lines in the first Brillouin zone. Arrows represent various possible optical transitions, with black arrows indicating transitions between bands that are highly probable. (b) The oscillator strengths of the possible transitions along high-symmetry lines in the first Brillouin zone (presented as purple bars).

absorption onsets are observed which correspond well to PR spectra as shown in Fig. 2. As the temperature increases, the onsets that correspond to transitions E_3 and E_G shift to lower energies. Moreover, the rate of shift of the absorption edge of E_G is bigger than for E_3, which results in the overlap of the E_G transition over E_3. In the case of the E_1 absorption onset and the signal from E_2, the change in energy induced by temperature is very small. It should be noted that the unambiguous determination of the absorption edge is difficult for $MnPS_3$; therefore, photoreflectance measurements give clearer results. Increasing the distance between the orbitals of the atoms that make up the material, *i.e.*, increasing the lattice constant,

reduces the energy gap. The temperature evolution of the lattice constants is discussed later.

In Fig. 5(a), we illustrate the temperature dependence of the optical transitions (E_1, E_2, E_3, and E_G). Filled points represent data obtained from the PR and Aspnes fitting methods, whereas empty points correspond to the optical absorption results. The temperature evolution of the E_3 and E_G transitions shows a decrease, with a distinct change in slope near the Néel temperature of approximately 78 K, resulting in two separate decreasing segments. In the temperature range of 20–80 K, the E_G transition redshifts from 2.90 to 2.80 eV according to the PR results, and from 2.895 to 2.81 eV according to the absorption results, indicating an average change of 15.4×10^{-4} eV K^{-1}. For the E_3 transition, the energy decreases from 2.66 eV to 2.62 eV (PR) and from 2.65 eV to 2.60 eV (absorption) within the same temperature range, resulting in an average change of 7.0×10^{-4} eV K^{-1}. For the optical transition E_2, the temperature dependence was determined only through absorption measurements, as the corresponding resonance in PR was visible only below 30 K. The optical transition E_2, observed in absorption across the entire temperature range, appears to not shift on the energy scale. For the E_1 transition, the energy surprisingly increases within the 20–80 K range, from 1.81 eV to 1.85 eV (PR) and from 1.75 eV to 1.76 eV (absorption), yielding an average increase of 4.2×10^{-4} eV K^{-1}. Above the Néel temperature (78 K), a decrease in energy is observed for all transitions, though the rate of decrease is smaller than below T_N. The average rates of decrease above T_N are as follows: 0.45×10^{-4} eV K^{-1} for E_1, 3.5×10^{-4} eV K^{-1} for E_3, and 13.75×10^{-4} eV K^{-1} for E_G.

To determine the transition temperature from the temperature-dependent PR spectra, we calculated the derivative of the energy-temperature curves, as shown in Fig. 5(b). It is clearly evident that the slope of the temperature evolution of the transitions changes near the Néel temperature, indicating that the position of the energy transition serves as a good marker for the magnetic phase transition in this material. The temperature evolution of the PR broadening parameter (Γ) is presented in Fig. S4 in the ESI.† A change in the slope of the PR broadening parameter for each transition can be observed around the Néel temperature of $MnPS_3$, suggesting that Γ can serve as an optical marker of the magnetic phase transition in this material (refer to the derivative $d\Gamma/dT$ in Fig. S4 in the ESI†).

The prominent reflections, as observed in Fig. 7(a), were identified as originating from the brass measuring table. The background signal detected below 20 degrees was attributed to the presence of Kapton foil in the cryostat's construction. The analysis of the diffraction reflections indicated a positional shift, signifying a change in the lattice constant, as illustrated in Fig. S5 (ESI†).

Due to the limited intensity of the reflections, the Rietveld refinement was deemed impractical. Instead, the lattice parameters of $MnPS_3$ were determined using Bragg's law. The most intense reflections evident in the measured patterns (Fig. 6(a)), specifically those corresponding to the (400), (310) and (001) planes, were used to derive the lattice parameters a, b, and c, respectively.
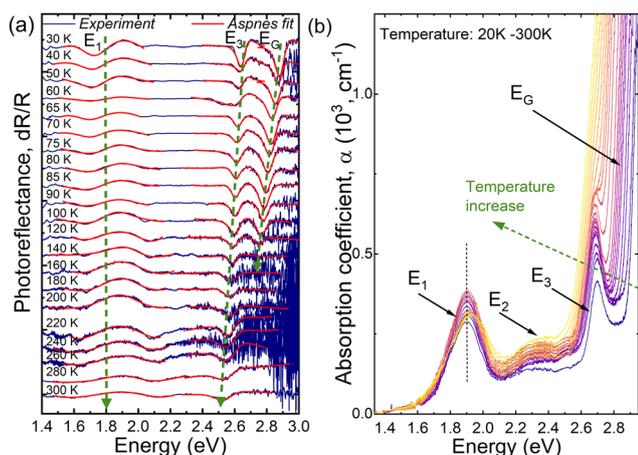

Fig. 4 (a) Temperature dependence of photoreflectance spectra with Aspnes fits (red lines) of $MnPS_3$ for optical transitions, and (b) temperature-dependent absorption of $MnPS_3$.
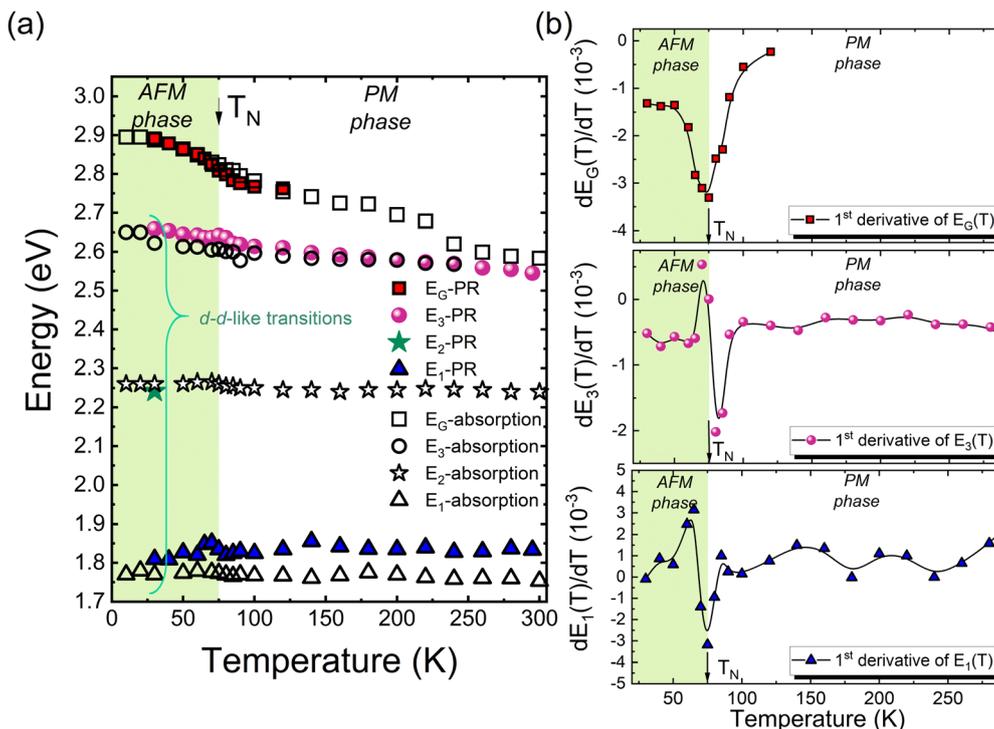
This journal is © The Royal Society of Chemistry 2025

J. Mater. Chem. C, 2025, **13**, 9194–9203 | **9199**

Fig. 5 (a) The energy of optical transitions observed for MnPS$_3$ as a function of temperature. Filled symbols represent the energies of transitions E_1, E_2, E_3, and E_G obtained from photoreflectance measurements, while empty symbols denote these transitions as determined by absorption measurements. (b) The gradient of the calculated energy-temperature curve used to determine the magnetic transition temperature from the temperature-dependent spectra.

Considering a monoclinic crystal system, the β angle was fixed at 107.35° as referenced in the JCPDF card no. 00-033-0903.

The influence of temperature variation on the lattice parameters of the unit cell is depicted in Fig. 6(b). A general decrease in the lattice parameters was observed with increasing temperature. Notably, around 70 K, a significant alteration was observed, associated with a magnetic phase transition that resulted in distinct changes in the lattice constants a, b, and c. The derived crystal parameters are summarized in Table S1 in the ESI.† The modification of lattice parameters in MnPS$_3$ has a pronounced impact on its band gap, primarily due to the effects of lattice expansion, which generally correlates with a change in the band gap energy. As temperature increases, the increased interatomic distances weaken the electron-nucleus interactions, potentially leading to a reduction in the binding energy of the electrons in the valence band. Furthermore, the enhanced lattice vibrations can intensify electron–phonon coupling, resulting in significant changes to the electronic band structure and, consequently, the band gap.

In order to understand the experimentally observed trends in temperature dependencies occurring during the transition through the magnetic phase transition temperature, we conducted theoretical calculations for a system mimicking a paramagnetic (PM) state.

While DFT is a powerful tool for computing the ground-state properties of electronic systems, it does not formally allow for the direct calculation of a paramagnetic state.[65] This limitation arises because DFT operates within a zero-temperature, static

framework and is fundamentally based on pure quantum states with well-defined spin configurations. Paramagnetism, by contrast, is a statistical phenomenon characterized by dynamically disordered local magnetic moments, typically observed at finite temperatures. However, it is possible to approximate the effects of such spin disorder within DFT by constructing supercells with randomized or disordered local magnetic moment orientations. This approach enables the calculation of the electronic structure in the presence of magnetic disorder, providing valuable insights into how the lack of magnetic order influences the system's band structure and density of states. While this method does not reproduce the full thermodynamic nature of a paramagnetic state, it offers a practical route to exploring the interplay between magnetic disorder and electronic properties within a static DFT framework.

For a 3 × 3 × 2 supercell, we randomly assigned the directions of the net magnetic moment on each ion, ensuring that they averaged to zero across the entire supercell and retained their magnitudes (a schematic representation of the compared phases is shown in Fig. 7(b)). We then applied a band-unfolding procedure to compare the resulting spectral functions to bands of the AFM-Néel phase in the primitive cell. Due to the high computational cost associated with a large supercell featuring non-collinear magnetism, we limited our calculations to the band structure along the typical M–Γ–K directions for hexagonal 2D systems, with $k_z = 0.0$.

As shown in Fig. 7(a), states predominantly built from manganese 3d-states exhibit "broadening" in the PM phase,
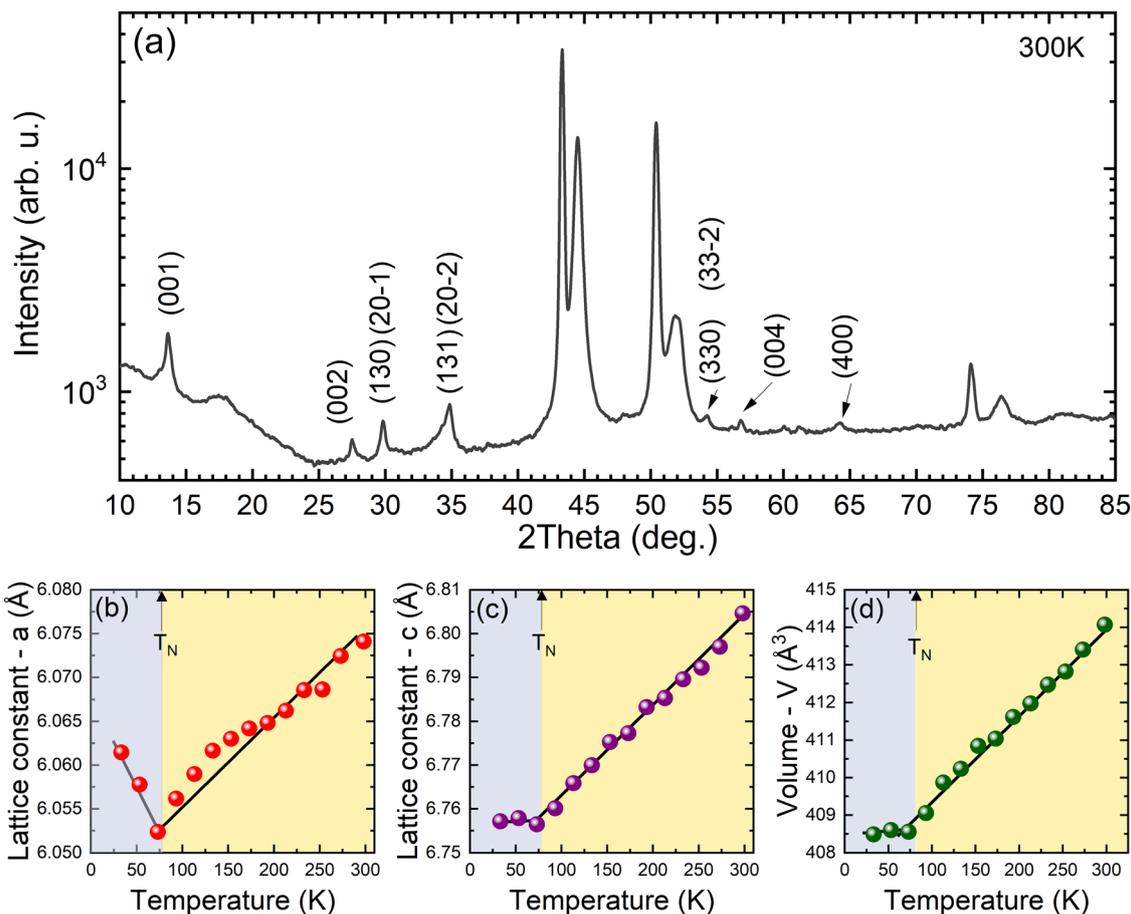
9200 | *J. Mater. Chem. C*, 2025, **13**, 9194–9203

This journal is © The Royal Society of Chemistry 2025

Fig. 6 (a) XRD pattern of bulk MnPS$_3$ material taken at 300 K. From temperature-dependent XRD measurements, the following parameters were determined as functions of temperature: (b) the a lattice constant, (c) the c lattice constant, and (d) the volume of the unit cell.
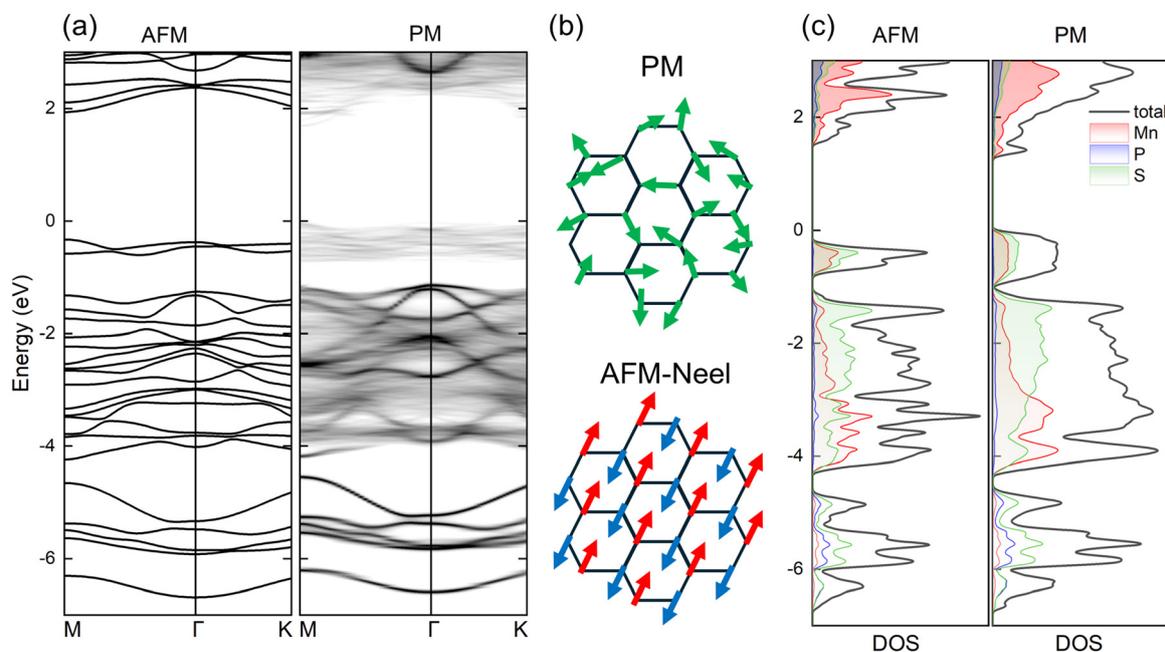

Fig. 7 (a) Theoretical effective electronic band structures for the AFM and PM phases, respectively. (b) A schematic illustrating these magnetic orderings. (c) Density of states with projections onto Mn, P, and S atomic states for both phases.

though this effect occurs primarily as a function of the wave vector. This effect is most prominent for conduction bands, which are purely (3d) in character, as well as for two isolated highest valence bands, where the contribution of these states is significant (see Fig. 7(c)). Between -1 eV and -4.5 eV, p states of sulphur hybridizing with manganese states are observed. In this energy range, despite slight broadening, the band dispersion remains distinct and similar to that in the AFM phase. Finally, in the range between -4.5 eV and -7 eV, sulphur and phosphorus states are precisely mirrored in both phases. Thus, these theoretical results seem to support the lack of significant changes in the observed optical transitions. In this material, the transition from the AFM phase to the PM phase does not lead to sudden changes in the electronic band structure a shifts in optical transitions. Any significant alterations observed are attributed to changes in the crystal lattice parameters. Consequently, it is the modifications in lattice parameters that drive these noticeable electronic variations, not the magnetic transition alone.

4 Conclusions

This study focused on the optical and structural properties of the antiferromagnetic semiconductor $MnPS_3$, providing essential insights into its behavior at varying temperatures and its potential roles in spintronics and optoelectronics. We identified significant optical transitions (E_1, E_2, E_3, and E_G) and observed that the E_1 transition increased in energy with temperature, contrasting with the downward shifts observed for E_3 and E_G. The position of E_2 remained unchanged during the temperature evolution. Complementary X-ray diffraction analysis demonstrated that variations in lattice parameters with temperature are closely related to these optical transitions, particularly around the Néel temperature (78 K). This emphasizes that lattice changes play a crucial role in the electronic behavior of $MnPS_3$, beyond the effects of the magnetic phase transition. Theoretical calculations corroborate our experimental observations, suggesting that the transition from the antiferromagnetic to paramagnetic phase does not significantly impact the electronic structure; rather, it is the alterations in lattice parameters that predominantly influence the optical transitions.

In summary, this research deepens our understanding of the magneto-optical characteristics of $MnPS_3$ and underscores the significance of lattice dynamics in 2D materials, setting the stage for new applications and further explorations of other magnetic materials.

Data availability

Data for this article are available at ZENODO at **https://doi.org/10.5281/zenodo.14732296**.

Conflicts of interest

There are no conflicts to declare.

Acknowledgements

References

1 C.-A. Chuang, M.-H. Lin, B.-X. Yeh and C.-H. Ho, *RSC Adv.*, 2018, **8**, 2733.

2 Y.-C. Lin, H.-P. Komsa, C.-H. Yeh, T. Björkman, Z.-Y. Liang, C.-H. Ho, Y.-S. Huang, P.-W. Chiu, A. V. Krasheninnikov and K. Suenaga, *ACS Nano*, 2015, **9**, 11249.

3 M. Li, C.-Y. Lin, S.-H. Yang, Y.-M. Chang, J.-K. Chang, F.-S. Yang, C. Zhong, W.-B. Jian, C.-H. Lien, C.-H. Ho, H.-J. Liu, R. Huang, W. Li, Y.-F. Lin and J. Chu, *Adv. Mater.*, 2018, **30**, 1803690.

4 C.-H. Ho and J.-X. Li, *Adv. Opt. Mater.*, 2017, **5**, 1600814.

5 C.-H. Ho and Y.-C. Chen, *RSC Adv.*, 2013, **3**, 24896.

6 S. Y. Lim, K. Kim, S. Lee, J.-G. Park and H. Cheong, *Curr. Appl. Phys.*, 2021, **21**, 1.

7 J.-U. Lee, S. Lee, J. H. Ryoo, S. Kang, T. Y. Kim, P. Kim, C.-H. Park, J.-G. Park and H. Cheong, *Nano Lett.*, 2016, **16**, 7433.

8 K. Hwangbo, Q. Zhang, Q. Jiang, Y. Wang, J. Fonseca, C. Wang, G. M. Diederich, D. R. Gamelin, D. Xiao, J.-H. Chu, W. Yao and X. Xu, *Nat. Nanotechnol.*, 2021, **16**, 655.

9 K.-Z. Du, X.-Z. Wang, Y. Liu, P. Hu, M. I. B. Utama, C. K. Gan, Q. Xiong and C. Kloc, *ACS Nano*, 2016, **10**, 1738.

10 P. Joy and S. Vasudevan, *Phys. Rev. B:Condens. Matter Mater. Phys.*, 1992, **46**, 5425.

11 D. Mukherjee, P. M. Austeria and S. Sampath, *ACS Energy Lett.*, 2016, **1**, 367.

12 A. McCreary, J. R. Simpson, T. T. Mai, R. D. McMichael, J. E. Douglas, N. Butch, C. Dennis, R. Valdés Aguilar and A. R. Hight Walker, *Phys. Rev. B*, 2020, **101**, 064416.

13 H. Zhang, Z. Ni, C. E. Stevens, A. Bai, F. Peiris, J. R. Hendrickson, L. Wu and D. Jariwala, *Nat. Photonics*, 2022, **16**, 311.

14 R. Brec, D. M. Schleich, G. Ouvrard, A. Louisy and J. Rouxel, *Inorg. Chem.*, 1979, **18**, 1814.

15 K. Kim, S. Y. Lim, J. Kim, J.-U. Lee, S. Lee, P. Kim, K. Park, S. Son, C.-H. Park, J.-G. Park and H. Cheong, *2D Mater.*, 2019, **6**, 041001.

16 H. A. Saleh, S. E. El-Shafey, A. M. Abdel-karim, M. S. Tohamy and A. A. El-Meligi, *Phys. Scr.*, 2025, **100**, 025522.

17 D. Tezze, J. M. Pereira, Y. Asensio, M. Ipatov, F. Calavalle, F. Casanova, A. M. Bittner, M. Ormaza, B. Martín-García, L. E. Hueso and M. Gobbi, *Nanoscale*, 2022, **14**, 1165.

18 G. Ouvrard, R. Brec and J. Rouxel, *Mater. Res. Bull.*, 1985, **20**, 1181.

19 R. Brec, *Solid State Ionics*, 1986, **22**, 3.

20 R. Clement, L. Lomas and J. P. Audiere, *Chem. Mater.*, 1990, **2**, 641.

21 P. Fuentealba, L. Serón, C. Sánchez, J. Manzur, V. Paredes-Garcia, N. Pizarro, M. Cepeda, D. Venegas-Yazigi and E. Spodine, *J. Coord. Chem.*, 2014, **67**, 3894.

22 Y.-J. Sun, Q.-H. Tan, X.-L. Liu, Y.-F. Gao and J. Zhang, *J. Phys. Chem. Lett.*, 2019, **10**, 3087.

23 M. Birowska, P. E. Faria Junior, J. Fabian and J. Kunstmann, *Phys. Rev. B*, 2021, **103**, L121108.

24 X. Wang, J. Cao, Z. Lu, A. Cohen, H. Kitadai, T. Li, Q. Tan, M. Wilson, C. H. Lui, D. Smirnov, S. Sharifzadeh and X. Ling, *Nat. Mater.*, 2021, **20**, 964.

25 J. Song, Z. Fang, L. Liu, D. Wei and L. Yuan, *J. Mol. Model.*, 2023, **29**, 240.

26 Y. Zhou, K. He, H. Hu, G. Ouyang, C. Zhu, W. Wang, S. Qin, Y. Tao, R. Chen, L. Zhang, R. Shi, C. Cheng, H. Wang, Y. Liu, Z. Liu, T. Wang, W. Huang, L. Wang and X. Chen, *Laser Photonics Rev.*, 2022, **16**, 2100431.

27 H. Chu, C. J. Roh, J. O. Island, C. Li, S. Lee, J. Chen, J.-G. Park, A. F. Young, J. S. Lee and D. Hsieh, *Phys. Rev. Lett.*, 2020, **124**, 027601.

28 A. Harchol, S. Zuri, E. Ritov, F. Horani, M. Rybak, T. Woźniak, A. Eyal, Y. Amouyal, M. Birowska and E. Lifshitz, *2D Mater.*, 2024, **11**, 035010.

29 F. Kargar, E. A. Coleman, S. Ghosh, J. Lee, M. J. Gomez, Y. Liu, A. S. Magana, Z. Barani, A. Mohammadzadeh, B. Debnath, R. B. Wilson, R. K. Lake and A. A. Balandin, *ACS Nano*, 2020, **14**, 2424.

30 M. Gibertini, M. Koperski, A. F. Morpurgo and K. S. Novoselov, *Nat. Nanotechnol.*, 2019, **14**, 408.

31 D. Li, Y. Xu, J. Guo, F. Zhang, Y. Zhang, J. Liu and H. Zhang, *Opt. Express*, 2022, **30**, 36802.

32 X. Hou, X. Zhang, Q. Ma, X. Tang, Q. Hao, Y. Cheng and T. Qiu, *Adv. Funct. Mater.*, 2020, **30**, 1910171.

33 S.-X. Zhao, J.-P. Wang, Y. Liu, H. Han, H. Li, J. Zhang, L. Zhen, Y. Li and C.-Y. Xu, *Adv. Funct. Mater.*, 2024, **34**, 2405882.

34 J.-T. Yang, C.-J. Xu, H.-J. Wang, Q. Min, S.-J. Luo, Y.-C. Xiong, W. Ren and C. Jing, *J. Phys.: Condens. Matter*, 2023, **35**, 395501.

35 R. Kumar, R. Naidu, M. P. Austeria and S. Sampath, *ECS Meet. Abstr.*, 2020, **MA2020-01**, 822.

36 V. G. Piryatinskaya, I. S. Kachur, V. V. Slavin, A. V. Yeremenko and Y. M. Vysochanskii, *Low Temp. Phys.*, 2012, **38**, 870.

37 J. Strasdas, B. Pestka, M. Rybak, A. K. Budniak, N. Leuth, H. Boban, V. Feyer, I. Cojocariu, D. Baranowski, J. Avila, P. Dudin, A. Bostwick, C. Jozwiak, E. Rotenberg, C. Autieri, Y. Amouyal, L. Plucinski, E. Lifshitz, M. Birowska and M. Morgenstern, *Nano Lett.*, 2023, **23**, 10342.

38 N. Sivadas, S. Okamoto and D. Xiao, *Phys. Rev. Lett.*, 2016, **117**, 267203.

39 P. Němec, M. Fiebig, T. Kampfrath and A. V. Kimel, *Nat. Phys.*, 2018, **14**, 229.

40 S. Mu, R. P. Hermann, S. Gorsse, H. Zhao, M. E. Manley, R. S. Fishman and L. Lindsay, *Phys. Rev. Mater.*, 2019, **3**, 025403.

41 D. Kriegner, K. Výborný, K. Olejník, H. Reichlová, V. Novák, X. Marti, J. Gazquez, V. Saidl, P. Němec, V. Volobuev, G. Springholz, V. Holý and T. Jungwirth, *Nat. Commun.*, 2016, **7**, 11623.

42 D. Zhang, K. Wang, S. Chen, L. Zhang, Y. Ni and G. Zhang, *Nanoscale*, 2023, **15**, 1180.

43 A. Manoogian and J. C. Woolley, *Can. J. Phys.*, 1984, **62**, 285.

44 L. Viña, S. Logothetidis and M. Cardona, *Phys. Rev. B:Condens. Matter Mater. Phys.*, 1984, **30**, 1979.

45 Y. Varshni, *Physica*, 1967, **34**, 149.

46 R. Pässler, *Phys. Status Solidi B*, 1997, **200**, 155.

47 K. P. O'Donnell and X. Chen, *Appl. Phys. Lett.*, 1991, **58**, 2924.

48 R. Kudrawiec and J. Misiewicz, Optical Modulation Spectroscopy, in *Semiconductor Research*, ed. A. Patane and N. Balkan, Springer Series in Material Science, 2012, vol. 150, pp. 99–124.

49 G. Kresse and J. F. Müller, *Comput. Mater. Sci.*, 1996, **6**, 15.

50 N. A. W. Holzwarth, A. R. Tackett and G. E. Matthews, *Comput. Phys. Commun.*, 2001, **135**, 329.

51 J. P. Perdew, K. Burke and M. Ernzerhof, *Phys. Rev. Lett.*, 1996, **77**, 3865.

52 H. J. Monkhorst and J. D. Pack, *Phys. Rev. B*, 1976, **13**, 5188.

53 M. Rybak, P. E. Faria Junior, T. Woźniak, P. Scharoch, J. Fabian and M. Birowska, *Phys. Rev. B*, 2024, **109**, 054426.

54 S. Grimme, J. Antony, S. Ehrlich and H. Krieg, *J. Chem. Phys.*, 2010, **132**, 154104.

55 S. L. Dudarev, G. A. Botton, S. Y. Savrasov, C. J. Humphreys and A. P. Sutton, *Phys. Rev. B:Condens. Matter Mater. Phys.*, 1998, **57**, 1505.

56 M. Gajdoš, K. Hummer, G. Kresse, J. Furthmüller and F. Bechstedt, *Phys. Rev. B:Condens. Matter Mater. Phys.*, 2006, **20**, 045112.

57 V. Popescu and A. Zunger, *Phys. Rev. B:Condens. Matter Mater. Phys.*, 2012, **85**, 085201.

58 Q. Zheng, *VaspBandUnfolding: A tool for band structure unfolding in VASP*, **https://github.com/QijingZheng/VaspBandUnfolding**, 2023.

59 I. Brotons-Alcázar, R. Torres-Cavanillas, M. Morant-Giner, M. Cvikl, S. Mañas-Valero, A. Forment-Aliaga and E. Coronado, *Dalton Trans.*, 2021, **50**, 16281.

60 D. Aspnes, *Surf. Sci.*, 1973, **37**, 418.

61 V. Grasso, F. Neri, P. Perillo, L. Silipigni and M. Piacentini, *Phys. Rev. B:Condens. Matter Mater. Phys.*, 1991, **44**, 11060.

62 A. M. Ummah, Y.-H. Peng and C.-H. Ho, *FlatChem*, 2023, **41**, 100536.

63 B. L. Chittari, Y. Park, D. Lee, M. Han, A. H. MacDonald, E. Hwang and J. Jung, *Phys. Rev. B*, 2016, **94**, 184428.

64 F. Wang, T. A. Shifa, P. Yu, P. He, Y. Liu, F. Wang, Z. Wang, X. Zhan, X. Lou, F. Xia and J. He, *Adv. Funct. Mater.*, 2018, **28**, 1802151.

65 I. Abrikosov, A. Ponomareva, P. Steneteg, S. Barannikova and B. Alling, *Curr. Opin. Solid State Mater. Sci.*, 2016, **20**, 85–106.

This journal is © The Royal Society of Chemistry 2025

J. Mater. Chem. C, 2025, **13**, 9194–9203 | **9203**